



Evolution of Turbulence in the Diurnal Warm Layer

AURÉLIE J. MOULIN, JAMES N. MOUM, AND EMILY L. SHROYER

College of Earth, Ocean, and Atmospheric Sciences, Oregon State University, Corvallis, Oregon

(Manuscript received 29 August 2017, in final form 18 December 2017)

ABSTRACT

The daily evolution of temperature, stratification, and turbulence in the diurnal warm layer is described from time series measurements at low to moderate winds and strong insolation in the equatorial Indian Ocean. At 2.0-m depth, turbulence dissipation rates (ϵ) decreased by two orders of magnitude over 1–2 h immediately after sunrise, initiated by stratification caused by penetrating solar radiation prior to the change in sign of net surface heat flux from cooling to warming. Decaying turbulence preceded a period of rapid growth, in which ϵ increased by two orders of magnitude over a few hours, and following which ϵ approached a daytime period of near-steady state. Decay and growth rates predicted by a simplified turbulence model are consistent with those observed. During the daytime period of near-steady state, asymmetric temperature ramps were associated with enhanced ϵ , supporting the interpretation that this period represents a balance between buoyancy and shear production associated with a shear-driven response to trapping of momentum within the diurnal warm layer.

1. Introduction

Upper ocean heat content changes daily due to radiative forcing from the sun that creates a thin diurnal warm layer (DWL) extending several meters beneath the sea surface. While sea surface temperature (SST) controls the instantaneous air-sea turbulent heat flux, upper ocean heat content provides a diurnally varying heat reservoir that regulates the phase between solar heat flux and the diurnal SST cycle. The thickness and average temperature of this reservoir, which constitutes the DWL, depend on net surface heating, wind speed, and subsurface ocean mixing (Price et al. 1986; Fairall et al. 1996a; Kawai and Wada 2007).

Daytime increases in near-surface temperature cause near-surface vertical stratification (Fig. 1), which is diffused by vertical mixing. Diffusion of heat happens slowly during the day but then rapidly upon the onset of nighttime cooling and convectively driven mixing (e.g., Anis and Moum 1994). The daily cycle of heating and mixing serves to progressively increase upper ocean heat content by 20 MJ m^{-2} over the top 10 m during the 5 days shown in Fig. 1, equivalent to several tenths of a degree Celsius. This heat may later be transferred back to the atmosphere during periods of strong surface forcing from westerly wind bursts associated with the Madden–

Julian oscillation (MJO) in the equatorial Indian Ocean (Moum et al. 2014), for example, or may even contribute to driving synoptic atmospheric storms, including tropical cyclones (Emanuel 1999). Accurate representation of diurnal variability in the ocean is therefore important in simulation of lower-frequency atmospheric signals (e.g., Lee and Liu 2005; Solomon and Jin 2005; Danabasoglu et al. 2006; Seo et al. 2009; Bellenger et al. 2010).

The developing stratification within the DWL can have competing influences on turbulent mixing. On the one hand, stratification increases the gravitational stability of the system, thereby dampening turbulence. For example, turbulence has been shown to decay by an order of magnitude when the near-surface stratifies, either through surface heating (Brainerd and Gregg 1993; Caldwell et al. 1997) or precipitation (Smyth et al. 1997). At the same time, increased stratification in the DWL is known to trap wind-driven momentum at the base of the surface mixed layer forming a diurnal jet (Thorpe 1978; Price et al. 1986; Cronin and Kessler 2009), with velocity anomalies up to 0.19 m s^{-1} (Kudryavtsev and Soloviev 1990). Additionally, observations (Callaghan et al. 2014; Sutherland et al. 2016) have shown that within this diurnal jet turbulence is enhanced relative to depths below the DWL.

The enhancement of shear associated with the diurnal jet provides an energy source for turbulence production, an example of which is provided by Pham et al. (2017), who propose that DWL shear acts as the trigger to the deep

Corresponding author: Aurélie J. Moulin, ajmoulin.ocean@gmail.com

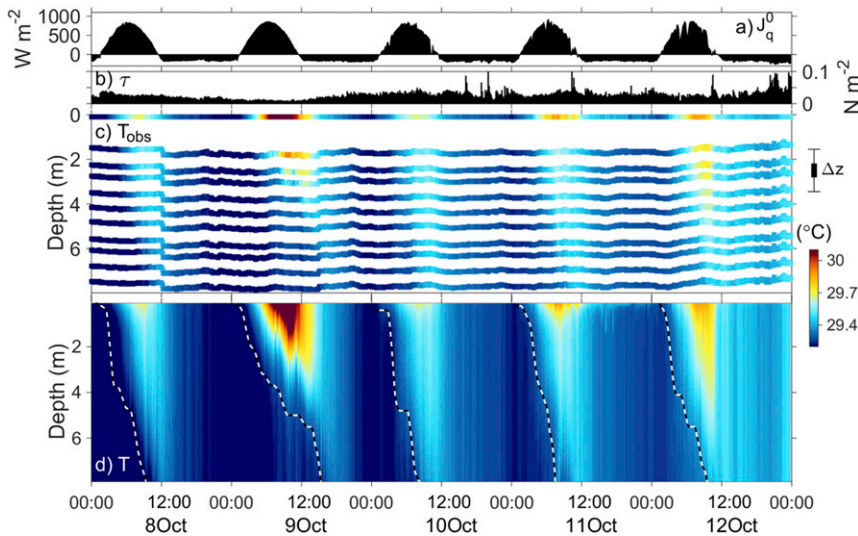


FIG. 1. Detailed temperature structure between 8 and 12 Oct 2011. (a) Net surface heat flux (J_q^0), (b) wind stress (τ), (c) observed temperature time series (10-min averages) at the sea surface and 10 depths in the upper 8.0 m, and (d) the gridded temperature (appendix A) showing the daily growth and diffusion of the diurnal warm layer. Total range in sensor depths on 10-min time periods is indicated by the thick black bar to the right of (c); whiskers represent the depth variations on a 3-s time scale. The dashed line in (d) represents the depth of the DWL. Time is in UTC (local time is UTC+6).

cycle of turbulence below the equatorial mixed layer. The mechanisms leading to reduced turbulent kinetic energy (TKE) dissipation may vary. For example, [Smyth et al. \(1997\)](#) and [Callaghan et al. \(2014\)](#) attribute turbulence decay to the interruption of the downward advection of convectively generated TKE at the surface by stratification capping associated with rainfall and surface heating, respectively. In contrast, in the cases presented by [Sutherland et al. \(2016\)](#), the reduction of TKE dissipation ε was associated with a decrease in the local shear production of turbulence due to enhanced stratification. In all of these examples, the time-evolving spatial patterns of turbulence in the upper ocean are directly linked to surface forcing with direct implications for air-sea interactions through control on sea surface temperature by subsurface mixing.

Here, we use time series data from the equatorial Indian Ocean to examine the detailed evolution of temperature T and ε within the DWL under light to moderate wind forcing and clear sky conditions (Fig. 1). Our observations show a repeated cycle in ε over the course of 5 days that were representative of these atmospheric conditions. An initial decay of ε at sunrise, which is likely caused by suppression of convection associated with the nascent DWL, is followed by a period of growth in ε through development of the diurnal jet as stratification, and presumably shear, builds in the DWL. Later in the afternoon, shear production and buoyancy suppression roughly balance one another, leading to a near-steady state in ε . Details of the measurements and analysis methods (section 2) are followed by a summary of the observations of temperature

(section 3) and turbulence (section 4). We then provide a quantitative evaluation of decay and growth rates of turbulence via an evolution equation for ε (section 5). We close with a short discussion of these results (section 6).

2. Measurements

The principal observations used in this study were acquired in October 2011 at 0° , 80.5°E during the Dynamics of the MJO field campaign (DYNAMO; [Moum et al. 2014](#)) in the equatorial Indian Ocean from a bow-mounted chain of temperature and conductivity sensors (Table 1, Fig. 2). The ship was also equipped with a full suite of meteorological sensors from which surface heat, momentum, and buoyancy fluxes were derived ([De Szoeke et al. 2015](#)). Ancillary measurements include those from a shipboard acoustic Doppler current profiler and the Chameleont turbulence profiler ([Moum et al. 1995](#)).

The ship maintained position and was oriented into a strong and relatively steady surface flow that brought

TABLE 1. Details of T -chain instruments.

	DYNAMO	
	Tpods	CTD
Number of sensors	8	2
Sampling frequency	10 Hz	0.33 Hz
Depth range	1.5–6.6 m	4.2, 7.6 m
Sensor Separation		0.2–0.7 m
Location		0° , 80.5°E

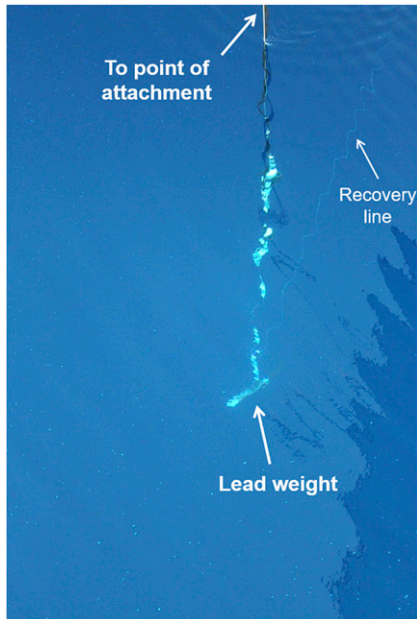


FIG. 2. Thermistor chain deployed from the bow of *R/V Revelle* during DYNAMO. The chain was outfitted with two CTDs and eight thermistors as listed in Table 1.

undisturbed fluid past the bow-mounted sensor suite. Profilers tethered to the fantail are not well suited to measure the details of upper ocean structure because of contamination by the ship's wake and bow thrusters. For example, simultaneous profiles of temperature from the bow thermistor chain (*T*-chain) and Chameleon profiler deployed from the stern of the *R/V Revelle* show significant differences in the upper 10 m (Fig. 3). Stratification clearly evident in *T*-chain data is absent in the Chameleon record. The uncontaminated *T*-chain measurements are essential to resolve development of the DWL, which is often shallower than a few meters.¹ Eight fast thermistors (FP07, sampling at 10 Hz) and two CTDs (SBE37, sampling at 3 s) were distributed on the bow chain between 1.5 and 7.5 m (Table 1, Fig. 2). SST was measured by a thermistor mounted into a brass body and sealed in a buoyant Tygon tube towed beside the ship at nominally 0.05-m depth (Fairall et al. 1997). Depths of sensors suspended on the bow chain varied (Fig. 1c) according to changes in relative flow speed of

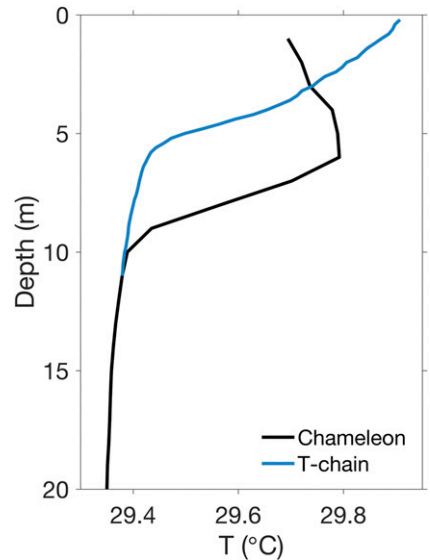


FIG. 3. Simultaneous temperature profiles in the upper ocean from the Chameleon profiler (black) and from the *T*-chain (blue). Note that three additional CTDs were installed on the *T*-chain at 8.6, 9.7, and 10.7 m at the above time, which occurred after the time period presented in Fig. 1.

ship and currents (± 0.5 m) as well as to motion induced by surface gravity waves (± 1.0 m).

3. Evolution of $T(z)$ in the DWL

Much of the DYNAMO record is influenced by freshwater lenses formed by precipitating convective systems of the MJO (Moum et al. 2014), which have a strong effect on near-surface stratification. No freshwater lenses were detected from 8 to 12 October 2011, as these days preceded the first convective systems of the 2011 MJO season. During this period, wind speeds ranged from 2.3 to 8.7 m s^{-1} , and daily averaged values of wind stress τ varied from 0.01 to 0.04 N m^{-2} , representing low to moderate winds. Clouds were present less than 15% of the day, so that the time period was characterized by nearly clear sky conditions.

The diurnal variations in the vertical structure of T followed a clear pattern. The example shown in Fig. 4 is representative of the 5 days examined here. Nighttime cooling mixed the upper 8 m, leaving a T profile with no vertical structure at 0000 UTC in Fig. 4b. Daytime heating progressively increased the heat content in the upper 8 m by increasing the temperature at all depths, most strongly at the surface. The daytime profiles (0200–1000 UTC, corresponding to 0800–1600 local time) showed roughly an exponential decrease with depth indicating weak mixing and a dominant contribution from penetrating solar radiation (usually

¹The depth of the DWL was defined as the greatest depth at which the time rate of change in temperature T_t exceeded $1.3 \times 10^{-5} \text{ }^{\circ}\text{C s}^{-1}$. This threshold level was based on the average heating rate of SST 1 h after sunrise. The DWL depth was shallowest at sunrise when it was reset to the surface and deepest near sunset. MLD was defined as the depth where $T(z)$ deviated from its surface value by 0.25°C . MLD was deepest at sunrise and shallowest around local noon.

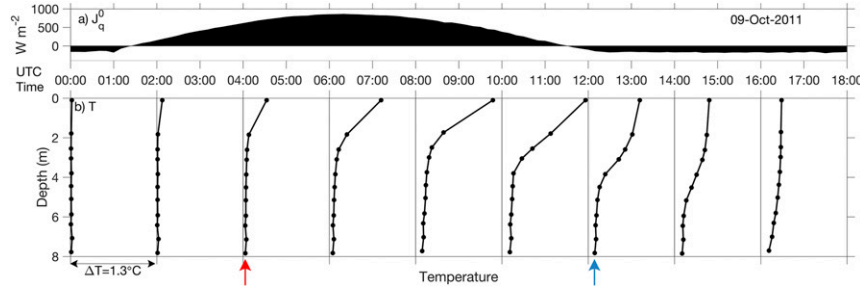


FIG. 4. Evolution of (a) J_q^0 and (b) the observed temperature profiles (10-min averages) on 9 Oct 2011. Profiles are shown every other hour to emphasize vertical structure. Red and blue arrows denote the profile examples shown in Fig. A1.

approximated as an exponential shape decreasing with depth; Ohlmann and Siegel 2000). As surface heating weakened in the afternoon, the near-surface T decreased, as did the stratification. At 1200 and 1400 UTC, the profile exhibited a characteristic hyperbolic tangent structure with a well-mixed layer near the surface indicative of intensified mixing.

We take advantage of this evolution of vertical structure and fit exponential and hyperbolic tangent curves to observed temperature profiles as detailed in appendix A. These fits allow for calculation of a smoothly varying vertical derivative T_z on 10-min intervals. This vertical derivative is then used for estimation of ε (appendices B and C). Note that the curvature of T is poorly constrained above 1.5 m because of a lack of sensors, leading to a high uncertainty

in T_z during the day when stratification develops near the surface. Because of the contribution of T_z to our estimate of ε (appendix B), estimates above 1.5 m are considered less reliable than below and are not used for quantitative scalings presented in section 5.

4. Stratification and turbulence within the diurnal warm layer

The depth and magnitude of the daily cycle in the DWL (Fig. 5) reflected the variability in wind stress with daily ranges in SST (shown here with no cool skin correction) varying from 0.5° to 1.3°C . The largest daily range in SST corresponded to the weakest winds (Figs. 5b,c). Peak values of N^2 at 2.0 m varied from 2 to $10 \times 10^{-4}\text{s}^{-2}$ in the late solar afternoon during this 5-day time span

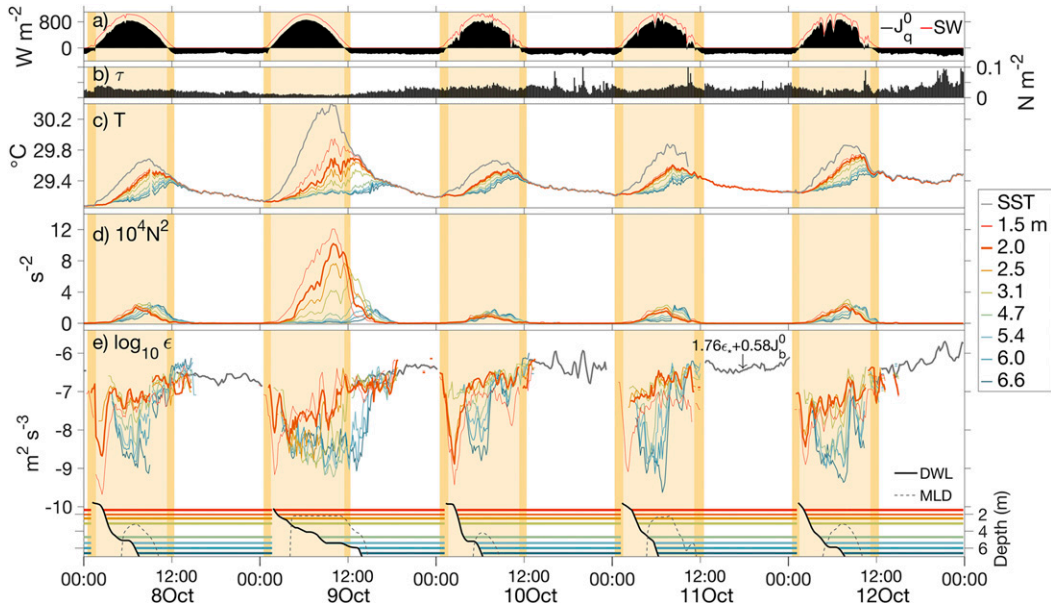


FIG. 5. Time series of (a) J_q^0 (black) and SW (red), (b) τ , (c) thermistor temperatures (SST; gray), (d) N^2 , and (e) ε . The dark gray line in (e) shows a scaling for nighttime dissipation, $1.76\varepsilon_* + 0.58J_q^0$, where $\varepsilon_* = u_*^2/(\kappa z)$ (Lombardo and Gregg 1989). The horizontal colored lines at the base of (e) represent times when individual sensors were within the DWL (black). Dashed lines indicate MLD. Vertical yellow bands mark times when $J_q^0 > 0$ (warming); orange bands reflect times when SW > 0 and $J_q^0 < 0$. Parameter ε was not computed during weakly stratified or convectively unstable conditions (i.e., when $T_z > -10^{-3}\text{ }^\circ\text{C m}^{-1}$).

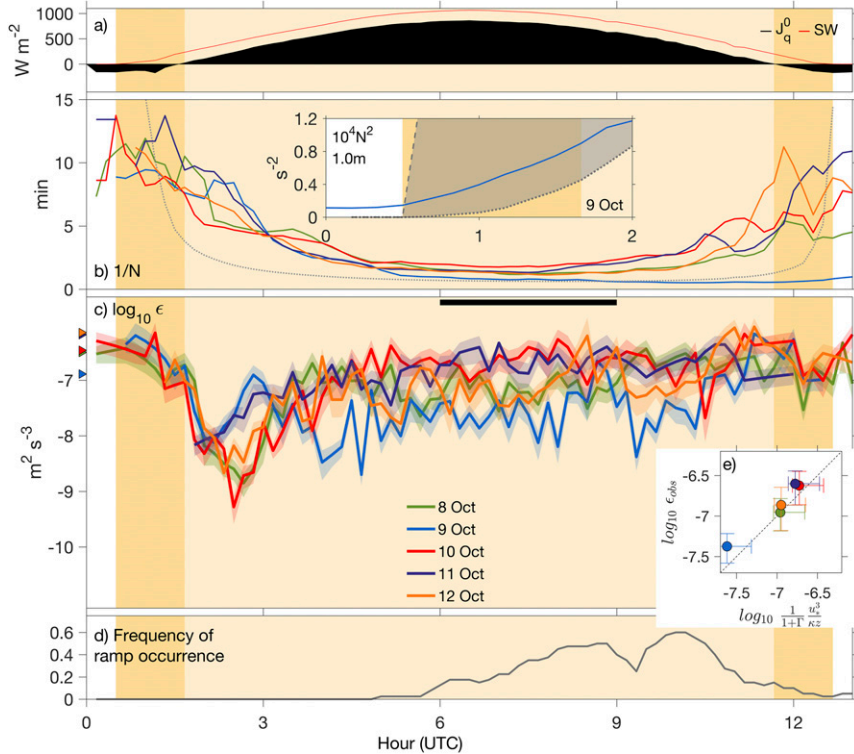


FIG. 6. Daily evolution of (a) the composite J_q^0 (black) and SW (red), (b) $1/N$ observed at 2.0 m (solid) and inferred from the solar flux divergence [using the transmission profile of Ohlmann and Siegel (2000), dotted], (c) ϵ at 2.0 m with 95% confidence limits (shading), and (d) frequency of ramp occurrence based on T_z and skewness of T_x . The background shading is as defined in Fig. 5. The inset in (b) shows N^2 at 1.0 m evaluated as $N^2 = g\alpha\Delta T/\Delta z$ from T observed at 0.05 and 1.5 m (blue) and estimated from solar flux divergence [Ohlmann and Siegel (2000), dotted; Jerlov (1976), dashed]. Triangles on the left-hand side of (c) indicate nighttime scaling from Lombardo and Gregg (1989). The scatterplot in (e) compares ϵ derived from Eq. (5) to the observed estimate calculated over the time period 0600–0900 UTC, indicated by the black horizontal bar in (c). Error bars were calculated from the 90% confidence interval on ϵ (see appendix B).

(Fig. 5d). Here, the buoyancy frequency, $N^2 = -(g/\rho)\rho_z$, where ρ_z is the vertical derivative of ρ . Variability in N^2 above 2.0 m was significantly greater; however, the uncertainty in the curvature of T over this range limits quantitative comparisons. Stratification continued to develop at depth progressively later in the day.

The stratification induced by the divergence of the penetrating solar radiation [the product of the surface-incident shortwave radiation (SW), and the time-dependent, depth-dependent solar transmission profile] appears to play a determining role in the decay of nighttime convective turbulence *before* the change in sign of the net surface heat flux J_q^0 (Fig. 5e). (Note that in Figs. 5 and 6, we make the distinction between $\text{SW} > 0$, $J_q^0 > 0$ shown in yellow shading and $\text{SW} > 0$, $J_q^0 < 0$ shown in darker orange shading.) A detail showing buoyancy frequency N^2 when $\text{SW} > 0$ but while $J_q^0 < 0$ (inset to Fig. 6b) shows that the stratification just beneath the surface

begins to increase from very small values before J_q^0 becomes positive (fluxes are positive into the ocean). This increase must be due to the solar flux divergence. During this time, the measured stratification calculated from differencing observations at 0.05 and 1.5 m is indeed consistent with that calculated by integrating the one-dimensional vertical heat equation in time with no mixing, and using as bounds solar transmission profiles from Ohlmann and Siegel (2000) and Jerlov (1976) (Fig. 6b, inset).

A daily repeated signature in the temporal evolution of near-surface turbulence is clear in Fig. 5. Upon sunrise, the following trends are apparent in the upper 2.5 m:

- 1) Coincident with increased stratification following sunrise but before J_q^0 changed sign, ϵ began to decrease, at first slowly but subsequently by two orders of magnitude between 0030 and 0200 UTC.

- 2) This decay was followed by a rapid increase of ε by two orders of magnitude over roughly 2 h.
- 3) After the period of rapid growth, the rate of increase in ε slowed or plateaued in the afternoon as the diurnal warm layer deepened.

Given the consistent nature of these trends, we seek a framework to model the signals in the following section.

5. Time-dependent representation of ε at 2.0 m

We consider the observed temporal changes in ε at 2.0 m in terms of the evolution equation for TKE. Time series above 2.5 m (that are regularly within the DWL once it develops; Fig. 5e) seem to behave synchronously compared to deeper sensors (that are often near or within the mixed layer; Fig. 5e). Neglecting transport (or TKE flux) terms, changes to TKE are determined by sources and sinks: shear production (P), buoyancy production (B), and dissipative losses (ε):

$$\frac{\partial}{\partial t} \underbrace{\frac{1}{2} \overline{u'_i u'_j}}_{\text{TKE}} = - \underbrace{\overline{u'_i u'_j} \frac{\partial u_i}{\partial x_j}}_P - \underbrace{\frac{g}{\rho} \overline{u'_3 \rho'}}_B - \varepsilon, \quad (1)$$

where g is the gravitational acceleration, ρ is density, and u_i, u_j are velocity components with the third component defined as vertical. Overbars denote mean quantities, and primed quantities denote turbulent fluctuations. Following Smyth et al. (1997), we develop a time-dependent equation for a scaled TKE u^2 by approximating $(1/2)\overline{u'_i u'_j}$ as $3/2u^2$, scaling the Reynolds stress as $\overline{u'_i u'_j} = C_{uv}u^2$, and scaling the background shear $\partial u_i / \partial x_j$ as S (a positive scale for the background shear). A summary of Reynolds stress estimates from large-eddy simulations in a stratified jet (Pham and Sarkar 2011), direct numerical simulations in a channel flow (Kim et al. 1987), and, on geophysical scales, from measurements in an estuary with a tidal bore (Simpson et al. 2004) suggest $C_{uv} \approx 0.3$. This value is consistent with usage in generic length-scale equations for geophysical turbulence models (Umlauf and Burchard 2003). We proceed using $C_{uv} = 0.3$.

Here, we have assumed that shear production always acts as a source of TKE. Since we limit the consideration here to stable stratification, B is always a TKE sink and is represented by $B = \Gamma\varepsilon$ (Osborn 1980) with an assumed constant mixing efficiency $\Gamma = 0.2$ (Moum 1996; Gregg et al. 2018). With these simplifications, Eq. (1) leads to a time-dependent equation for u^2 that depends on ε ,

$$\frac{d}{dt} \frac{3}{2} u^2 = C_{uv} u^2 S - \varepsilon(\Gamma + 1). \quad (2)$$

Note that the minus sign in P [Eq. (1)] cancels in our scaled version Eq. (2) since $\overline{u'_i u'_j}$ has the opposite sign, on average, as $\partial u_i / \partial x_j$ in sheared flows, resulting in $P > 0$.

We then relate u to ε via the inviscid scale relation $\varepsilon = (C_\varepsilon u^3)/l$, where l is the length scale of the energy-containing eddies and C_ε is roughly 0.5 (Smyth et al. 1997). In a stratified fluid where buoyancy limits l , the appropriate choice for l is the Ozmidov scale, $L_o = \sqrt{\varepsilon}/N^3$. With these simplifications, a time-dependent equation for ε can be derived as

$$\frac{d\varepsilon}{dt} = \frac{2}{3} \varepsilon [C_{uv}S - C_\varepsilon^{2/3} N(1 + \Gamma)]. \quad (3)$$

We continue with the assumption that we can neglect the time dependence of N . That is, although $N(t) \neq$ constant, we assume its temporal evolution is slow compared to that of $\varepsilon(t)$.

Equation (3) has a general solution of the form

$$\varepsilon(t) = C_o e^{t/\gamma}, \quad (4)$$

where C_o is a constant of integration and $\gamma = [(2/3)(C_{uv}S - \alpha N)]^{-1}$, $\alpha = C_\varepsilon^{2/3}(1 + \Gamma) \approx 0.75$. This solution results in decay of ε when $\gamma < 0$, or $C_{uv}S < \alpha N$, and growth when $\gamma > 0$, or $C_{uv}S > \alpha N$. The equality $C_{uv}S = \alpha N$ represents a singularity in γ corresponding to $S = 2.5N$ and a pure steady state. This equality separates growth from decay regimes (Fig. 7). For comparison, the value $S = 2N$, the instability condition for stratified shear flow, is also noted in Fig. 7.

A direct measure of N is derived from our thermistor chain measurements. The range of values (from Fig. 6) for each of decay, growth, and steady-state periods is noted in Table 2. However, we have no direct measure of velocity above ~ 10 m, thus limiting our ability to constrain S . Instead, we base estimated shear ranges in the three regimes on the results of Sutherland et al. (2016, see their Fig. 14a that also separates into growth, decay, and steady-state conditions below 4-m depth). Sutherland et al. (2016) show diurnally varying averaged values of S normalized by $a^{1/3}u_*/\kappa z$, where $\kappa = 0.4$ is von Kármán's constant, $u_* = \sqrt{\tau/\rho_w}$ is a friction velocity, and ρ_w is the density of seawater. The constant a is estimated to range between 0.5 and 2, and we take $a^{1/3}$ to be 1. Because of potential sampling bias with their uppermost velocity bins, we base our estimates of $S\kappa z/u_*$ using values below 3.5 m depth. During the decay period, Sutherland et al. (2016) show $S\kappa z/u_*$ values less than 1, possibly close to 0. Their value of $S\kappa z/u_*$ increases during the growth regime to roughly 2–4 and continues to increase later in the day when steady state is reached (when values are near 4–5). These

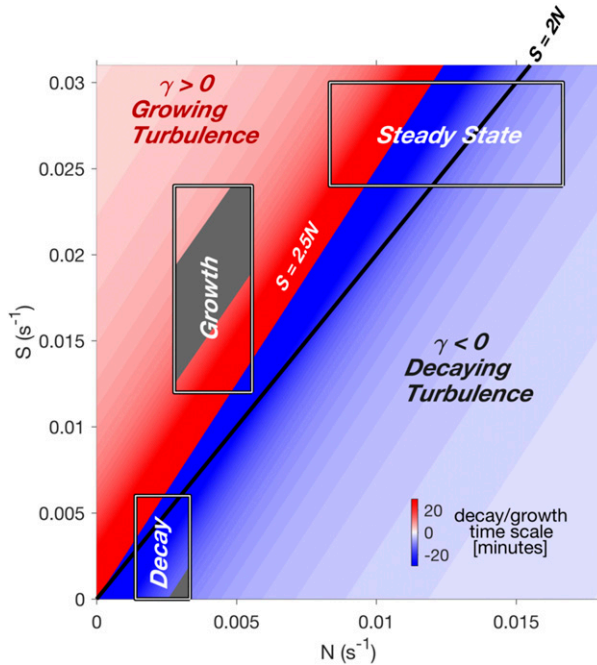


FIG. 7. Variation of time scales γ over realistic ranges of N and S . Red depicts growth and blue depicts decay. The boxes bound regimes represented by the values of N and S listed in Table 2. Gray shaded areas show overlap regions of γ within the boxes and γ_{obs} .

values (Table 2) are not intended to be exact and instead provide guidance in interpreting Fig. 7. During the period of our observations, the average value of $u_*/\kappa z$ was 0.006 s^{-1} .

In the next sections we assess Eq. (4) using measured values of N and presumed values of S (Table 2) and using the averaged value of $u_*/\kappa z$ to estimate γ in comparison to observed decay and growth rates seen in Fig. 6c and to investigate the role of shear instability during the steady state.

a. Decay

In the upper 2.5 m, turbulence decays shortly after the sun rises, but before J_q^0 changes sign to heat the sea surface. The decay period continued past the transition to positive J_q^0 . The rate of decay of $\varepsilon(t)$ is estimated as the e -folding time scale γ_{obs} over the decay time period by fitting a line to $\ln \varepsilon$. Estimates of γ_{obs} for the 5 days range from -13 to -8 min with an average value of -10 min (with the negative sign indicating decay in time).

The Businger–Dyer (Businger et al. 1971; Dyer 1974) representation of Monin–Obukhov (MO) similarity theory (Monin and Obukhov 1954) predicts that $S \sim u_*/(\kappa z)$ above the depth defined by the MO length scale $L = u_*^3/(\kappa B^0)$, where B^0 is the value of buoyancy production B at $z = 0$. At the beginning of the decay period, L is -1 to -4.5 m depending on the particular day, which is in the range of the uppermost three thermistors. However, the near-surface restratification by the solar flux divergence is not accounted for by MO similarity theory for shear scaling. During the decay period, stratification builds in a very shallow layer near the surface, initially above our uppermost sensor. In this case, the value of S at our uppermost sensors may be significantly less than the Businger–Dyer prediction because of momentum trapping by very near-surface stratification. The range $S = (0 - 1)u_*/(\kappa z)$ is consistent with this argument and our interpretation of Sutherland et al. (2016) (Table 2). The box bounding the range of S , N from Table 2 for the decay period (Fig. 7) includes our upper bound estimates of γ_{obs} .

b. Growth

During the period of rapid increase in ε noted in Fig. 6, our estimates of γ_{obs} range from 7 to 15 min, with a mean value of 11 min. Using the values of S , N deduced for the growth period in Table 2 to compute γ , the box denoted “Growth” in Fig. 7 includes the full range of our observed estimates γ_{obs} .

c. Steady state

The period of rapid growth ended at roughly 0400–0500 UTC (1000–1100 local time), after which the turbulence was nearly steady. In this case, Eq. (2) reduces to

$$C_{\text{uw}} u^2 S = (1 + \Gamma) \varepsilon. \quad (5)$$

For steady boundary layer flows, the Reynolds stress $\overline{u'_i u'_j}$ is typically scaled as u_*^2 (Tennekes and Lumley 1972; Fairall et al. 1996b; Perlin et al. 2005) and S as $u_*/(\kappa z)$. The resultant estimates of $\varepsilon = [1/(1 + \Gamma)][u_*^3/(\kappa z)]$ yield a reasonable representation of observed values as depicted in Fig. 6e. This is consistent with measurements beneath the DWL (Lombardo and Gregg 1989). We revisit this scaling and result in section 6.

TABLE 2. Summary of ranges of values used to estimate γ .

	Decay	Growth	Steady state
$N (\text{min}^{-1})$ (from Fig. 6)	1/12–1/5	1/6–1/3	1/2–1
$S/u_*/\kappa z$ (from Sutherland et al. 2016, Fig. 14)	0–1	2–4	4–5
γ_{obs} (min)	$-10 [-13, -8]$	11 [7, 15]	

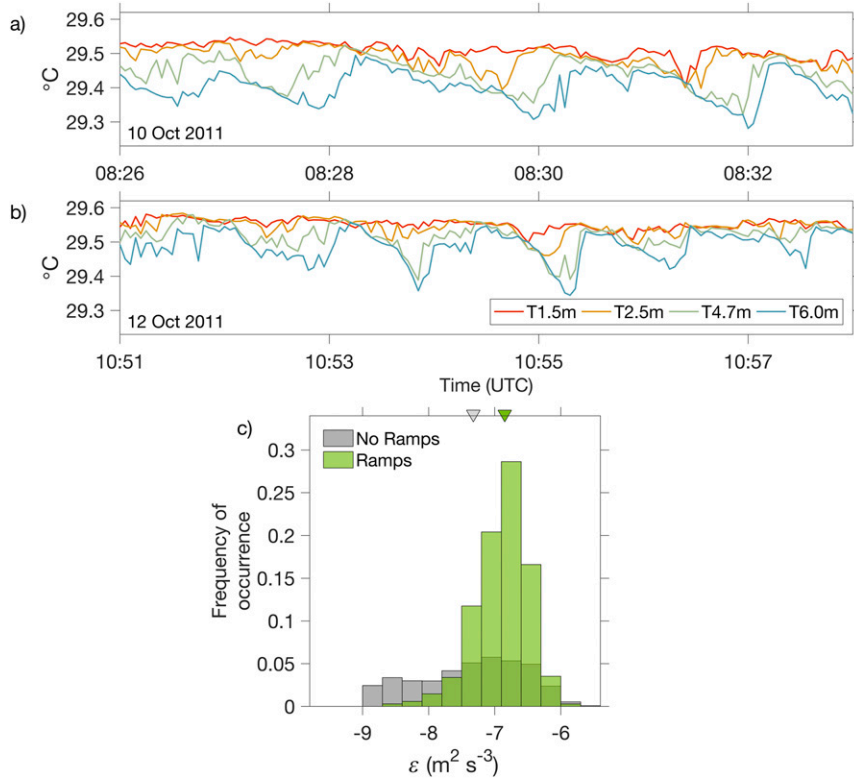


FIG. 8. (a),(b) Time series of temperature at four depths showing examples of temperature ramps, and (c) normalized distribution of ε in the presence (green, $N = 697$) and absence (gray, $N = 5063$) of ramps. Median values are indicated by inverted triangles at the top of (c). The Kolmogorov-Smirnov test confirms a statistically significant difference between distributions ($p \ll 10^{-4}$).

6. Discussion

The decay of ε beneath the DWL following the onset of surface heating has been described by Brainerd and Gregg (1993). A similar scenario was described by Smyth et al. (1997) following the capping of the ocean's surface by freshwater from rain squalls. In both cases the subsurface was decoupled from surface forcing by a rapid increase in near-surface stratification, and they both derived a time scale for the decay of ε from a reduced TKE equation in the absence of shear production as in section 5a. Smyth et al.'s (1997) value for the turbulence decay time scale of $0.7N^{-1}$ is comparable to our estimate.

Our measurements differ from those described above in that these data are much closer to the sea surface, where a priori we did not expect $S = 0$ at any time. The observations of Sutherland et al. (2016) show that daytime values of S are significantly $>u_*/(\kappa z)$ within the DWL and are close to $u_*/(\kappa z)$ at night. Our observations during the ε decay period arguably point toward a surface confinement of shear when near-surface temperatures warm significantly more than those below $\approx 1\text{ m}$. At this time of day, as much as 75% of the solar heat is deposited in the upper meter [based on the Ohlmann and Siegel

(2000) solar transmission profile]. This stratification is above the depths of all of the measurements used to estimate ε and shown in Figs. 5 and 6. In this case, the decay of turbulence immediately following sunrise must be due to the absence of both TKE flux from above and local shear production in the presence of limiting stratification at and above sensor depths.

Subsequent stages of growth and steady state require a source of turbulence. An additional observation suggests this is due to shear instability. During daytime, temperature time series were marked by the presence of asymmetric structures (Figs. 8a,b) that were more commonly observed from late morning to late afternoon (Fig. 6d). Similar features were termed ramps by Thorpe (1978), who suggested that these are the signatures of Kelvin-Helmholtz instability created by wind-generated shear in the presence of stable heating. In our data, temperature ramps² were observed near

²Temperature ramps were identified by the skewness of the lateral temperature gradient T_x . Three-second temperature time series were first low-pass-filtered at 0.066 Hz (15 s) to remove surface wave signals, and skewness of T_x was then computed from hour-long time records. Ramps were identified by $T_z > 0.02^\circ\text{C m}^{-1}$ and hourly skewness of $T_x > 0.35$.

the surface at the end of the ε growth period (Fig. 6d); thereafter, they were observed progressively deeper over the top 7 m and with increasing frequency until N^2 decreased at day's end. These features were not observed at night when vertical stratification was negligible. The measured ε was greater in the presence than in the absence of ramps (Fig. 8c). We suspect, then, that the turbulence observed during the steady-state period was generated through shear instability and breaking Kelvin–Helmholtz billows.

We have argued that our estimates of γ based on parameter values listed in Table 2 are consistent with γ_{obs} , as indicated in Fig. 7 for periods of both decay and growth. We have also indicated that our estimates of ε based on thermistor measurements from our bow chain are consistent with nearby estimates based on shear probe measurements from our profiler Chameleon (appendix C). As well, during the steady state period, the range of observed values of N and estimates of S in Table 2 overlap the $\gamma = 0$ regime in Fig. 7, and are therefore consistent with our proposed scenario.

However, a significant inconsistency arises in our application of Eq. (5), where we found that our estimate of ε is $\approx [1/(1 + \Gamma)][u_*^3/(\kappa z)]$. This requires $S = u_*/\kappa z$. Since N is constrained by our observations, this value of S would move the box bounding the steady state in Fig. 7 to a level that suggests fairly rapid decay. Sutherland et al. (2016) suggest S is much larger than this during steady state (Table 2). Moreover, during the steady-state period, the value of $2N$ at 2.0 m depth is observed to be $(2\text{--}5) \times u_*/(\kappa z)$. In this case, if we assume that $S = 2N$, close to the value for marginal stability evidenced by the apparent observed Kelvin–Helmholtz billows during the steady-state period, then the observed ε is inconsistent with that presented in section 5c and estimated by Eq. (5). This physical state does not seem to be consistent with the assumptions leading to the balance proposed in Eq. (1), namely, that we can neglect the TKE flux terms in this balance. However, it is likely that the generation site for the turbulence is below 2.0 m (Fig. 6c), that is, the turbulence measured at 2.0 m was generated below this depth and advected to the point of measurement following shear instability focused below 2.0 m. In this case the balance in Eq. (1) must include vertical advection of TKE, $\overline{u'_3}(\partial/\partial z)(1/2)\overline{u'_i u'_i}$, a term notoriously difficult to assess. The apparent agreement of scaled and observed values of ε in Fig. 6e may then be either fortuitous or an effective representation of the near-field vertical redistribution of the turbulence, and only source and sink terms need be considered, as in Eq. (1). Another possible explanation (suggested by a reviewer of this paper) that addresses the inconsistency we have identified is that the solar flux divergence contributes a buoyancy sink in addition to the mixing (or increase in

potential energy brought about by $\Gamma\varepsilon$). This larger B would balance Eq. (5) with larger S .

The depths of DWL and mixed layer in relation to our thermistors is shown in Fig. 5e. The flaw in our definition of mixed layer depth (MLD) is obvious, as the mixed layer was clearly stratified. However, these definitions of DWL and MLD help to distinguish the behavior of $\varepsilon(t)$ within the DWL and above the MLD from that below. The behavior of $\varepsilon(t)$ discussed in section 4 roughly holds for all of the sensors above the MLD, although we have only emphasized that at 2.0 m in Fig. 6c. Below the MLD the behavior is less clear, in part because the lack of stratification very early in the day precludes estimating ε then. But once the MLD shallowed above sensor depth, ε decayed and remained small during the day, increasing only when the DWL again deepened, and reaching a maximum when MLD was deeper than the sensors. At this time, the warming associated with the increase in ε was presumably due to mixing down of warm water from above.

While we have identified three principal regimes in the evolution of daytime turbulence within the DWL, there are several aspects that we have not addressed, all of which can be seen in Figs. 5 and 6. First, during the decay period a consistent pattern emerges in which there appear to be two stages of decay; slowly, immediately after sunrise and then more rapidly following the change in sign of J_q^0 . Second, for at least 2 of the 5 days examined, there was a slow increase in ε during the period we have identified as steady state. Finally, there is a brief period of decay at the end of the heating cycle.

In sum, we have shown a consistent pattern of mixing in the diurnal warm layer, in this case associated with the strong insolation of the tropics. While the signal may be more subtle away from the tropics, the general pattern ought to hold elsewhere, save for a poleward-increasing Coriolis veering of the diurnal jet. The phasing between air–sea fluxes and the ocean's response, which in part is determined by this repeatable cycle in subsurface mixing, may need to be considered in improvements to diurnal warm layer parameterizations that include more realistic representations of mixing.

Acknowledgments. This work was funded by the National Science Foundation (1059055) and by the Office of Naval Research (N0001-10-1-2098). Data used in this research are available on the DYNAMO website (https://www.eol.ucar.edu/field_projects/dynamo). M. Neeley-Brown, R. Kreth, and A. Perlin provided technical support. The surface flux dataset obtained on the R/V *Revelle* for this experiment was kindly provided by Jim Edson, Simon de Szoëke, and Chris Fairall. We acknowledge the constructive comments of Ren-Chieh Lien and an anonymous reviewer.

APPENDIX A

Continuous Temperature Profiles from Point Measurements

All fast thermistors were reconciled with SBE37 measurements during periods of nighttime convection, when it was assumed that all sensors recorded the same temperature, by applying constant offsets of up to 0.05°C to fast thermistors as needed. All data were then averaged onto a common 600-s time grid and regressed at each time step onto two types of vertical curves based on observed conditions (as described in section 3) and mean-square error (MSE) between the measurements and fits. Regressions on the selected forms were used to create a gridded temperature product with 10-min resolution in time and 0.1-m resolution in depth (Fig. 1d). This gridded product was used to calculate layer depths (see below) and vertical derivatives of temperature (T_z), which are used in calculation of χ and ε_χ .

Over roughly half of the day, we applied a nonlinear regression of data to the form

$$T_{\exp}(z) = \beta_1 e^{-z\sqrt{\omega/(2\beta_2)}} + \beta_3 e^{-\text{Tr}(z)\cdot z} + \beta_4, \quad (\text{A1})$$

where $\omega = 1/12\text{ h}$ and $\text{Tr}(z)$ is the profile of solar attenuation. The above form was inspired by the solution to the one-dimensional heat equation with time-dependent solar heating, steady cooling, and constant diffusivity (Moulin 2016; Dake and Harleman 1969). The first exponential in Eq. (A1), with amplitude β_1 , represents the influence of turbulent mixing; the second exponential, with amplitude β_3 , represents the decay of the penetrating solar radiation. Parameter β_2 has units of meters squared per second and is equivalent to a turbulent diffusivity in the full solution, and β_4 represents the temperature below the DWL to which the exponential profile asymptotes as z becomes large relative to the two decay scales. The fit is initialized with parameters $\beta_{[1,2,3,4]}$ set to $[0.2; 10^{-5}; 0.01; T_{7.6\text{m}}]$ and constrained by all subsurface measurements.

When T_{\exp} was not characteristic of the measured temperature profile (e.g., compare Figs. A1a and A1b), we applied a nonlinear regression to the form

$$T_{\tanh}(z) = \alpha_1 \tanh[\alpha_2(z + \alpha_3)] + \alpha_4. \quad (\text{A2})$$

For T_{\tanh} , we initialize the regression with parameters $\alpha_1\text{--}\alpha_4$ determined using the measured temperature profile. Parameter α_1 was set to half of the temperature difference across the profile. Parameter α_2 was set to the inverse depth of the maximum T_z (based on differences between sensor pairs). Parameters α_3 and α_4 were based

on the average depth and temperature near the maximum T_z , respectively.

The above fits were applied for depths greater than 1.75 m (i.e., between the location of the first and second fast thermistor), and thus hold for gradients used in calculation of χ at depths greater than or equal to 2.0 m (i.e., at all locations except the uppermost thermistor). Above 1.75 m, we found that the curvature between the sea snake and the first thermistor was not always well modeled by the above descriptions. At these times, we applied an iterative process where the fits above were merged with an exponential fit constrained by the sea snake as well as subsurface sensors in order to minimize the total MSE. This process only influences the gradient at the uppermost fast thermistor and thus influences the magnitude (although not the overall evolution trend) in χ at this location.

The T_{\tanh} and T_{\exp} curves were selected based on time of day and the MSE between the regressions and the measurements. From 0000 to 0600 UTC, T_{\exp} was presumed more representative unless the MSE of T_{\tanh} was smaller. From 0600 to 2300 UTC, T_{\tanh} was presumed more representative unless the MSE of T_{\exp} was smaller. Each form accounted for roughly 50% of 10-min profiles over the 5-day period. Note that the curvature of T_{\tanh} around its inflection point yielded a better fit than T_{\exp} starting around 0600 UTC even in the absence of a mixed near-surface layer.

APPENDIX B

Mixing Estimates from Bow Chain Temperature Measurements

For isotropic turbulence, the dissipation of thermal variance (χ_T) can be calculated as

$$\chi_T = \langle 6D_T \rangle \int_0^\infty \Phi_{T_x}(k) dk, \quad (\text{B1})$$

where D_T is the thermal diffusivity, $\Phi_{T_x}(k)$ is the power spectrum of the horizontal derivative of temperature T_x , and k is the wavenumber. Within the inertial subrange $\Phi_{T_x}(k)$ follows (Batchelor 1959; Dillon and Caldwell 1980)

$$\Phi_{T_x}(k) = C_T \chi_T \epsilon^{-1/3} k^{1/3}, \quad (\text{B2})$$

where C_T is the Obukhov–Corrsin constant ($C_T = 0.4$; Sreenivasan 1996). Here, we use the inertial subrange of turbulence for scaling observed spectra to avoid contamination by surface gravity waves. Assuming that the turbulence diffusivity $K_T = \chi_T / 2T_z^2$ (Osborn and Cox 1972) is also equal to $K_\rho = \Gamma \epsilon / N^2$ (Osborn 1980), where

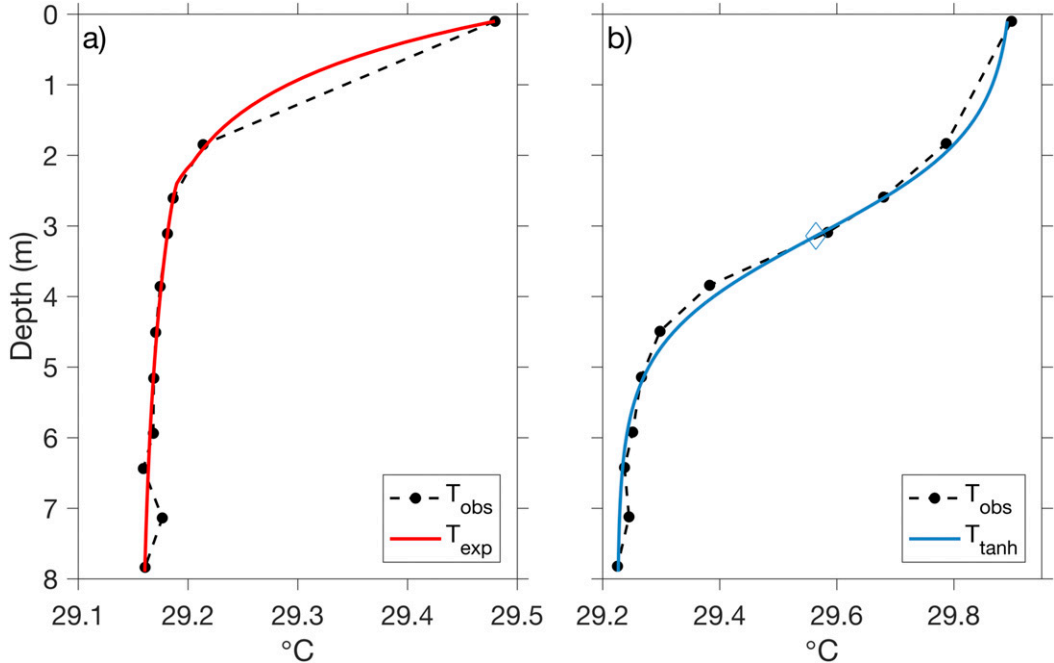


FIG. A1. Illustration of temperature profile regression forms from (a) T_{exp} inspired from the heat equation (red) regressed onto observations (black) and from (b) T_{tanh} derived from a hyperbolic tangent form (blue) regressed onto observations (black). The blue diamond represents the center of curvature of the tanh profile.

Γ is the mixing efficiency and N^2 is the buoyancy frequency, the spectrum becomes

$$\Phi_{T_x}(f) = (2\pi)^{4/3} C_T \left(\frac{2\Gamma T_z^2}{N^2} \right)^{1/3} \chi_T^{2/3} u^{-4/3} f^{1/3}, \quad (\text{B3})$$

where we have converted to frequency f space assuming $f = uk$, where u is the mean fluid velocity.

To estimate χ_T from the observed temperature time series, we first convert temporal derivatives to spatial derivatives using Taylor's hypothesis ($T_x = (1/u) dT/dt$; Taylor 1938) with u set to the depth-averaged current velocity between $z = 12$ – 16 m measured by the ship's ADCP. Temperature gradient spectra were then calculated and regressed onto a $+1/3$ slope over the frequency band 0.0183–0.0660 Hz (Fig. B1). This frequency band was chosen to avoid contamination by wind waves and swell. A 90% confidence interval on the regression coefficient was used to estimate upper and lower bounds on χ_T using Eq. (B3). A constant mixing efficiency $\Gamma = 0.2$ was used (Osborn 1980; Gregg et al. 2018). Examples of spectral fits for examples of both high and low χ from the bow chain measurements are shown in Fig. B1 together with confidence limits derived as indicated above. TKE dissipation was then estimated as $\varepsilon_\chi = (\chi_T N^2)/(2\Gamma T_z^2)$, where the subscript χ indicates that ε is derived from temperature microstructure rather than shear.

The above assumptions prohibit calculation of ε during convection, and ε_χ was not computed when $T_z > -10^{-3}$ °C m $^{-1}$. (Note that $T_z > 0$ corresponds to an unstable density profile over the observation time period when salinity was not an important contributor to density.) Values of ε exceeding $10^{-5.8}$ or smaller than 10^{-12} m 2 s $^{-3}$ were also removed. Collectively, removed data points account for roughly 60% of the total dataset.

The method outlined above follows directly from algorithms developed for processing of moored turbulence meters (χ pods) in the viscous-convective (Moum and Nash 2009) and inertial-convective subranges (Zhang and Moum 2010; Becherer and Moum 2017). The results have been validated against microstructure profiling measurements using shear probes by Perlis and Moum (2012) and Pujiana et al. (2018).

In the main text ε_χ has been replaced with ε for convenience.

APPENDIX C

Comparison of Bow Chain and Profiler Measurements of Turbulence

In Fig. C1, we compare the turbulent kinetic energy dissipation rate from the T-chain at 6.0–6.6 m, ε_χ , to Chameleon profiler estimates ε_{Sh} , based on airfoil probe measurements averaged between 8 and 10 m. This

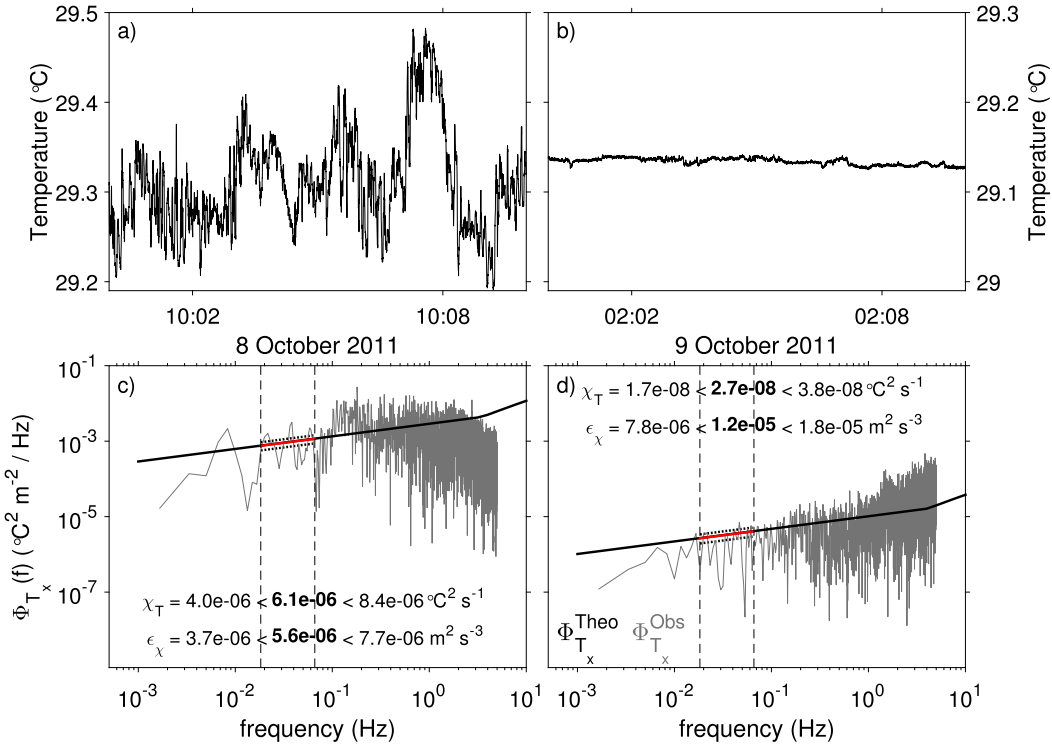


FIG. B1. Temperature time series and their derived turbulence quantities from spectral fits. (a),(b) Ten minutes of fast (10 Hz) temperature data from a thermistor at 6.0 m; (c),(d) spectra of T_x (gray) fit to the Batchelor spectrum (black) between frequencies 0.0183 and 0.066 Hz (dashed vertical lines). The resulting χ_T and ϵ_χ estimates are given in (c) and (d). Panels (a) and (c) represent an example of high temperature variance dissipation, and (b) and (d) represent an example of low temperature variance dissipation. The bounds represent 90% confidence based on the 90% range of fits indicated by the dotted lines bracketing the spectra.

Chameleon depth range was determined to be the shallowest range consistently outside the ship's wake. The profiler was deployed approximately 78 m downstream of the T -chain, corresponding to 1.5–2.0 min of

drift time, which is shorter than the time between Chameleon profiles (6–10 min).

The magnitude and variability of ϵ_χ and ϵ_{Sh} are roughly comparable (Fig. C1). The slight phase lag of ϵ_{Sh}

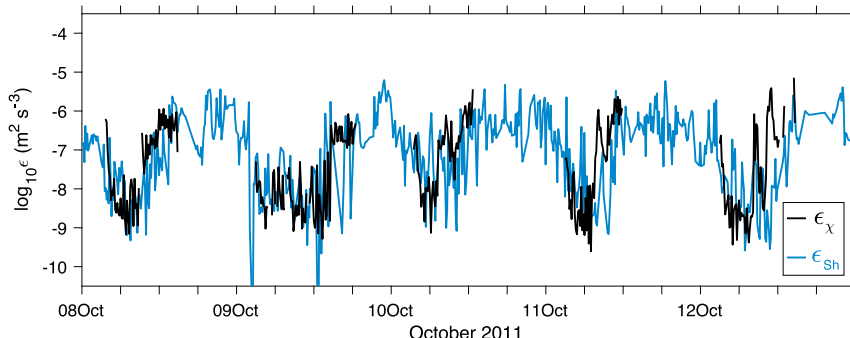


FIG. C1. Time series of the dissipation of turbulent kinetic energy evaluated from Chameleon shear probes, (ϵ_{Sh}), averaged between 8 and 10 m, and evaluated from T -chain (ϵ_χ) averaged between 6.0 and 6.6 m.

relative to ε_χ may be due to the depth-dependent time response of the turbulence to surface forcing.

REFERENCES

- Anis, A., and J. N. Moum, 1994: Prescriptions for heat flux and entrainment rate in the upper ocean during convection. *J. Phys. Oceanogr.*, **24**, 2142–2155, [https://doi.org/10.1175/1520-0485\(1994\)024<2142:PFHFAE>2.0.CO;2](https://doi.org/10.1175/1520-0485(1994)024<2142:PFHFAE>2.0.CO;2).
- Batchelor, G. K., 1959: Structure variation of convected quantities like temperature in turbulent fluid: Part 1. General discussion and the case of small conductivity. *J. Fluid Mech.*, **5**, 113–133, <https://doi.org/10.1017/S002211205900009X>.
- Becherer, J., and J. N. Moum, 2017: An efficient scheme for onboard reduction of moored χ pod data. *J. Atmos. Oceanic Technol.*, **34**, 2533–2546, <https://doi.org/10.1175/JTECH-D-17-0118.1>.
- Bellenger, H., Y. N. Takayabu, T. Ushiyama, and K. Yoneyama, 2010: Role of diurnal warm layers in the diurnal cycle of convection over the tropical Indian Ocean during MISMO. *Mon. Wea. Rev.*, **138**, 2426–2433, <https://doi.org/10.1175/2010MWR3249.1>.
- Brainerd, K. E., and M. C. Gregg, 1993: Diurnal restratification and turbulence in the oceanic surface mixed layer: 1. Observations. *J. Geophys. Res.*, **98**, 22 645–22 656, <https://doi.org/10.1029/93JC02297>.
- Businger, J. A., J. C. Wyngaard, Y. Izumi, and E. F. Bradley, 1971: Flux-profile relationships in the atmospheric surface layer. *J. Atmos. Sci.*, **28**, 181–189, [https://doi.org/10.1175/1520-0469\(1971\)028<0181:FFPITA>2.0.CO;2](https://doi.org/10.1175/1520-0469(1971)028<0181:FFPITA>2.0.CO;2).
- Caldwell, D., R.-C. Lien, J. N. Moum, and M. C. Gregg, 1997: Turbulence decay and restratification in the equatorial ocean surface layer following nighttime convection. *J. Phys. Oceanogr.*, **27**, 1120–1132, [https://doi.org/10.1175/1520-0485\(1997\)027<1120:TDARIT>2.0.CO;2](https://doi.org/10.1175/1520-0485(1997)027<1120:TDARIT>2.0.CO;2).
- Callaghan, A. H., B. Ward, and J. Vialard, 2014: Influence of surface forcing on near-surface and mixing layer turbulence in the tropical Indian Ocean. *Deep-Sea Res. I*, **94**, 107–123, <https://doi.org/10.1016/j.dsr.2014.08.009>.
- Cronin, M. F., and W. S. Kessler, 2009: Near-surface shear flow in the tropical Pacific cold tongue front. *J. Phys. Oceanogr.*, **39**, 1200–1215, <https://doi.org/10.1175/2008JPO4064.1>.
- Dake, J. M. K., and D. R. F. Harleman, 1969: Thermal stratification in lakes: Analytical and laboratory studies. *Water Resour. Res.*, **5**, 484–495, <https://doi.org/10.1029/WR005i002p00484>.
- Danabasoglu, G., W. G. Large, J. J. Tribbia, P. R. Gent, B. P. Briegleb, and J. C. McWilliams, 2006: Diurnal coupling in the tropical oceans of CCSM3. *J. Climate*, **19**, 2347–2365, <https://doi.org/10.1175/JCLI3739.1>.
- De Szoeke, S. P., J. B. Edson, J. R. Marion, C. W. Fairall, and L. Bariteau, 2015: The MJO and air-sea interaction in TOGA COARE and DYNAMO. *J. Climate*, **28**, 597–622, <https://doi.org/10.1175/JCLI-D-14-00477.1>.
- Dillon, T. M., and D. R. Caldwell, 1980: The Batchelor spectrum and dissipation in the upper ocean. *J. Geophys. Res.*, **85**, 1910–1916, <https://doi.org/10.1029/JC085iC04p01910>.
- Dyer, A. J., 1974: A review of flux-profile relationships. *Bound.-Layer Meteor.*, **7**, 363–372, <https://doi.org/10.1007/BF00240838>.
- Emanuel, K. A., 1999: Thermodynamic control of hurricane intensity. *Nature*, **401**, 665–669, <https://doi.org/10.1038/44326>.
- Fairall, C. W., E. F. Bradley, J. S. Godfrey, G. A. Wick, J. B. Edson, and G. S. Young, 1996a: Cool-skin and warm-layer effects on sea surface temperature. *J. Geophys. Res.*, **101**, 1295–1308, <https://doi.org/10.1029/95JC03190>.
- , —, D. P. Rogers, J. B. Edson, and G. S. Young, 1996b: Bulk parameterization of air-sea fluxes for Tropical Ocean-Global Atmosphere Coupled-Ocean Atmosphere Response Experiment. *J. Geophys. Res.*, **101**, 3747–3764, <https://doi.org/10.1029/95JC03205>.
- , —, A. B. White, J. B. Edson, and J. E. Hare, 1997: Integrated shipboard measurements of the marine boundary layer. *J. Atmos. Oceanic Technol.*, **14**, 338–359, [https://doi.org/10.1175/1520-0426\(1997\)014<0338:ISMOTM>2.0.CO;2](https://doi.org/10.1175/1520-0426(1997)014<0338:ISMOTM>2.0.CO;2).
- Gregg, M. C., E. A. D'Asaro, J. J. Riley, and E. Kunze, 2018: Mixing coefficients and mixing efficiency in the ocean. *Annu. Rev. Mar. Sci.*, **10**, 443–473, <https://doi.org/10.1146/annurev-marine-121916-063643>.
- Jerlov, N. G., 1976: *Marine Optics*. 2nd ed. Elsevier Oceanography Series, Vol. 14, Elsevier, 230 pp.
- Kawai, Y., and A. Wada, 2007: Diurnal sea surface temperature variation and its impact on the atmosphere and ocean: A review. *J. Oceanogr.*, **63**, 721–744, <https://doi.org/10.1007/s10872-007-0063-0>.
- Kim, J., P. Moin, and R. Moser, 1987: Turbulence statistics in fully developed channel flow at low Reynolds number. *J. Fluid Mech.*, **177**, 133–166, <https://doi.org/10.1017/S0022112087000892>.
- Kudryavtsev, V. N., and A. V. Soloviev, 1990: Slippery near-surface layer of the ocean arising due to daytime solar heating. *J. Phys. Oceanogr.*, **20**, 617–628, [https://doi.org/10.1175/1520-0485\(1990\)020<0617:SNSLOT>2.0.CO;2](https://doi.org/10.1175/1520-0485(1990)020<0617:SNSLOT>2.0.CO;2).
- Lee, T., and W. T. Liu, 2005: Effects of high-frequency wind sampling on simulated mixed layer depth and upper ocean temperature. *J. Geophys. Res.*, **110**, C05002, <https://doi.org/10.1029/2004JC002746>.
- Lombardo, C. P., and M. C. Gregg, 1989: Similarity scaling of viscous and thermal dissipation in a convecting surface boundary layer. *J. Geophys. Res.*, **94**, 6273–6284, <https://doi.org/10.1029/JC094iC05p06273>.
- Monin, A. S., and A. M. Obukhov, 1954: Basic laws of turbulent mixing in the atmosphere near the ground. *Tr. Geofiz. Inst., Akad. Nauk SSSR*, **24**, 163–187.
- Moulin, A. J., 2016: Evolution of turbulence, heat content, and freshwater lenses in the diurnal warm layer. Ph.D. thesis, Oregon State University, 189 pp.
- Moum, J. N., 1996: Energy-containing scales of turbulence in the ocean thermocline. *J. Geophys. Res.*, **101**, 14 095–14 109, <https://doi.org/10.1029/96JC00507>.
- , —, and J. D. Nash, 2009: Mixing measurements on an equatorial ocean mooring. *J. Atmos. Oceanic Technol.*, **26**, 317–336, <https://doi.org/10.1175/2008JTECHO617.1>.
- , —, M. C. Gregg, R. Lien, and M. E. Carr, 1995: Comparison of turbulence kinetic energy dissipation rate estimates from two ocean microstructure profilers. *J. Atmos. Oceanic Technol.*, **12**, 346–366, [https://doi.org/10.1175/1520-0426\(1995\)012<0346:COTKED>2.0.CO;2](https://doi.org/10.1175/1520-0426(1995)012<0346:COTKED>2.0.CO;2).
- , —, and Coauthors, 2014: Air-sea interactions from westerly wind bursts during the November 2011 MJO in the Indian Ocean. *Bull. Amer. Meteor. Soc.*, **95**, 1185–1199, <https://doi.org/10.1175/BAMS-D-12-00225.1>.
- Ohlmann, J. C., and D. A. Siegel, 2000: Ocean radiant heating. Part II: Parameterizing solar radiation transmission through the upper ocean. *J. Phys. Oceanogr.*, **30**, 1849–1865, [https://doi.org/10.1175/1520-0485\(2000\)030<1849:ORHIP>2.0.CO;2](https://doi.org/10.1175/1520-0485(2000)030<1849:ORHIP>2.0.CO;2).

- Osborn, T. R., 1980: Estimates of the local rate of vertical diffusion from dissipation measurements. *J. Phys. Oceanogr.*, **10**, 83–89, [https://doi.org/10.1175/1520-0485\(1980\)010<0083:EOOTLRO>2.0.CO;2](https://doi.org/10.1175/1520-0485(1980)010<0083:EOOTLRO>2.0.CO;2).
- , and C. S. Cox, 1972: Oceanic fine structure. *Geophys. Fluid Dyn.*, **3**, 321–345, <https://doi.org/10.1080/03091927208236085>.
- Perlin, A., and J. N. Moum, 2012: Comparison of thermal variance dissipation rates from moored and profiling instruments at the equator. *J. Atmos. Oceanic Technol.*, **29**, 1347–1362, <https://doi.org/10.1175/JTECH-D-12-00019.1>.
- , —, J. Klymak, M. Levine, T. Boyd, and P. Kosro, 2005: A modified law-of-the-wall applied to oceanic bottom boundary layers. *J. Geophys. Res.*, **110**, C10S10, <https://doi.org/10.1029/2004JC002310>.
- Pham, H. T., and S. Sarkar, 2011: Mixing events in a stratified jet subject to surface wind and buoyancy forcing. *J. Fluid Mech.*, **685**, 54–82, <https://doi.org/10.1017/jfm.2011.275>.
- , W. D. Smyth, S. Sarkar, and J. N. Moum, 2017: Seasonality of deep cycle turbulence in the eastern equatorial Pacific. *J. Phys. Oceanogr.*, **47**, 2189–2209, <https://doi.org/10.1175/JPO-D-17-0008.1>.
- Price, J. F., R. A. Weller, and R. Pinkel, 1986: Diurnal cycling: Observations and model of the upper ocean response to diurnal heating, cooling, and wind mixing. *J. Geophys. Res.*, **91**, 8411–8427, <https://doi.org/10.1029/JC091iC07p08411>.
- Pujiana, K., J. N. Moum, and W. D. Smyth, 2018: The role of subsurface turbulence in redistributing upper-ocean heat, freshwater, and momentum in response to the MJO in the equatorial Indian Ocean. *J. Phys. Oceanogr.*, **48**, 197–220, <https://doi.org/10.1175/JPO-D-17-0146.1>.
- Seo, H., S.-P. Xie, R. Murtugudde, M. Jochum, and A. J. Miller, 2009: Seasonal effects of Indian Ocean freshwater forcing in a regional coupled model. *J. Climate*, **22**, 6577–6596, <https://doi.org/10.1175/2009JCLI2990.1>.
- Simpson, J., N. Fisher, and P. Wiles, 2004: Reynolds stress and TKE production in an estuary with a tidal bore. *Estuarine Coastal Shelf Sci.*, **60**, 619–627, <https://doi.org/10.1016/j.ecess.2004.03.006>.
- Smyth, W. D., P. Zavialov, and J. N. Moum, 1997: Decay of turbulence in the upper ocean following sudden isolation from surface forcing. *J. Phys. Oceanogr.*, **27**, 810–822, [https://doi.org/10.1175/1520-0485\(1997\)027<0810:DOTITU>2.0.CO;2](https://doi.org/10.1175/1520-0485(1997)027<0810:DOTITU>2.0.CO;2).
- Solomon, A., and F. F. Jin, 2005: A study of the impact of off-equatorial warm pool SST anomalies on ENSO cycles. *J. Climate*, **18**, 274–286, <https://doi.org/10.1175/JCLI-3269.1>.
- Sreenivasan, K. R., 1996: The passive scalar spectrum and the Obukhov–Corrsin constant. *Phys. Fluids*, **8**, 189–196, <https://doi.org/10.1063/1.868826>.
- Sutherland, G., L. Marié, G. Reverdin, K. H. Christensen, G. Broström, and B. Ward, 2016: Enhanced turbulence associated with the diurnal jet in the ocean surface boundary layer. *J. Phys. Oceanogr.*, **46**, 3051–3067, <https://doi.org/10.1175/JPO-D-15-0172.1>.
- Taylor, G. I., 1938: The spectrum of turbulence. *Proc. Roy. Soc. London*, **164A**, 476–490, <https://doi.org/10.1098/rspa.1938.0032>.
- Tennekes, H., and J. L. Lumley, 1972: *A First Course in Turbulence*. MIT Press, 300 pp.
- Thorpe, S. A., 1978: The near-surface mixing layer in stable heating conditions. *J. Geophys. Res.*, **83**, 2875–2885, <https://doi.org/10.1029/JC083iC06p02875>.
- Umlauf, L., and H. Burchard, 2003: A generic length-scale equation for geophysical turbulence models. *J. Mar. Res.*, **61**, 235–265, <https://doi.org/10.1357/002224003322005087>.
- Zhang, Y., and J. N. Moum, 2010: Inertial-convective estimates of thermal variance dissipation rate from moored temperature measurements. *J. Atmos. Oceanic Technol.*, **27**, 1950–1959, <https://doi.org/10.1175/2010JTECHO746.1>.